

ADA044059

RADC-TR-76-348

12



*[Handwritten signature]*

## RESEARCH ON MATERIALS FOR HIGH POWER LASER WINDOWS

SEMI-ANNUAL TECHNICAL REPORT - NO. 2  
FOR THE PERIOD ENDING 31 MAY, 1976

CENTER FOR MATERIALS SCIENCE AND ENGINEERING  
MASSACHUSETTS INSTITUTE OF TECHNOLOGY  
CAMBRIDGE, MASSACHUSETTS 02139

Approved for public release; distribution unlimited

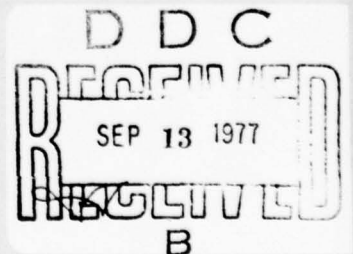
SPONSORED BY  
DEFENSE ADVANCED RESEARCH PROJECTS AGENCY

ARPA Order No. 2055

MONITORED BY  
ROME AIR DEVELOPMENT CENTER

AIR FORCE SYSTEMS COMMAND  
GRIFFISS AIR FORCE BASE, NEW YORK 13441

AD No.             
DDC FILE COPY





ARPA Order Number

2055

Contract Number

F19628-75-C-0191

Program Code Number

3 D 10

Principal Investigator

H. K. Bowen

(617) 253-6892

Name of Contractor

Massachusetts Institute

of Technology

RADC/ET Project Scientist

Harold Posen

(617) 861-3532

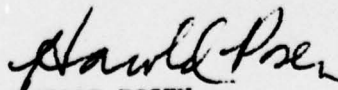
Effective Date of Contract

1 June 1975

Contract Expiration Date

28 February 1977

APPROVED:



HAROLD POSEN  
Contract Monitor



Unclassified

SECURITY CLASSIFICATION OF THIS PAGE (When Data Entered)

19 REPORT DOCUMENTATION PAGE		READ INSTRUCTIONS BEFORE COMPLETING FORM	
1. REPORT NUMBER RADC-TR-76-348	2. GOVT ACCESSION NO.	3. RECIPIENT'S CATALOG NUMBER	
4. TITLE (and Subtitle) RESEARCH MATERIALS FOR HIGH POWER LASER WINDOWS.		5. TYPE OF REPORT & PERIOD COVERED Semi-Annual report, No. 2 1 Dec 1975 - 31 May 1976	
7. AUTHOR(s) H. K. Bowen, R. M. Cannon, F. A. McClintock J. B. Vander Sande		8. CONTRACT OR GRANT NUMBER(s) F19628-75-C-0191	
9. PERFORMING ORGANIZATION NAME AND ADDRESS Massachusetts Institute of Technology Division of Sponsored Research 77 Mass. Ave., Cambridge, Mass. 02139		10. PROGRAM ELEMENT, PROJECT, TASK AREA & WORK UNIT NUMBERS ARPA Order No. 2055 61101E 562003-08	
11. CONTROLLING OFFICE NAME AND ADDRESS Defense Advanced Research Projects Agency 1400 Wilson Blvd. Arlington, VA. 22209		12. REPORT DATE Nov. 1976	
14. MONITORING AGENCY NAME & ADDRESS (if different from Controlling Office) Deputy for Electronic Technology (RADC/ETSO) Hanscom AFB, Mass. 01731 Monitor/ Harold Posen/ETSO		13. NUMBER OF PAGES	
16. DISTRIBUTION STATEMENT (of this Report) Approved for Public Release; distribution unlimited.		15. SECURITY CLASS. (of this report) Unclassified	
17. DISTRIBUTION STATEMENT (of the abstract entered in Block 20, if different from Report)		15a. DECLASSIFICATION/DOWNGRADING SCHEDULE	
18. SUPPLEMENTARY NOTES Research was sponsored by Defense Advanced Research Projects Agency, ARPA Order No. 2055.			
19. KEY WORDS (Continue on reverse side if necessary and identify by block number) Alkali Halides      Fracture      Grain Boundary Migration Alkaline Earth Halides      Flaw Analysis      Impurity Drag Recrystallization      Proof Testing Crack Coalescence      Subgrains			
20. ABSTRACT (Continue on reverse side if necessary and identify by block number) See attached page.			

DD FORM 1473  
1 JAN 73EDITION OF 1 NOV 65 IS OBSOLETE  
S/N 0102-014-6601Unclassified  
SECURITY CLASSIFICATION OF THIS PAGE (When Data Entered)

220 050

D D C  
RECEIVED  
SEP 13 1977  
B



Unclassified

SECURITY CLASSIFICATION OF THIS PAGE(When Data Entered)

The theory for impurity drag on the grain boundary mobility in KCl has been modified to include a secondary interaction force such as would result from a size misfit between the solute and matrix ions. For aliovalent solutes the interactions are coupled. Near the isoelectric temperature the modified drag is much greater than that predicted for an electrostatic interaction. A simplified model has been developed which indicates the conditions under which a fluctuation in velocity along a boundary may grow and cause a segment of boundary to make the transition between the low and high velocity modes.

Forged  $\text{CaF}_2$  samples have been examined by optical and transmission electron microscopy. There is a subgrain structure and the subgrain size decreases with increasing flow stress. Recrystallization which removes the subgrains can also occur during forging and during cooling. Recrystallization has been observed at temperatures as low as  $600^\circ\text{C}$  and is a serious problem above  $800^\circ\text{C}$  for pure samples.

The models for brittle fracture resulting from microcracking have been altered to include the effects of a free surface on the stresses around cracks. For the cases considered in which the same flaw distribution is assumed, the pressure of the free surface only lowers the ultimate stress by 10-20% and the stress for first cracking by a smaller amount. Consideration was given to the affect of grain shape on the fracture statistics. Methods of actually determining the parameters which characterize the distribution of microstrengths are discussed.

ACCESSION for	
NTIS	White Section <input checked="" type="checkbox"/>
DDC	Brief Section <input type="checkbox"/>
UNANNOUNCED	<input type="checkbox"/>
DISSEMINATION	
BY	
DISTRIBUTION/AVAILABILITY CODES	
DISC. AVAIL. AND FOR SPECIAL	
A	

Unclassified

SECURITY CLASSIFICATION OF THIS PAGE(When Data Entered)



## TABLE OF CONTENTS

	page
A. INTRODUCTION.....	5
B. MICROSTRUCTURE STUDIES.....	7
C. FRACTURE OF BRITTLE MATERIALS.....	35
D. REFERENCES.....	44



#### A. INTRODUCTION

The objectives of this program are to conduct research on processing and microstructure relations on materials suitable for infrared windows and to develop design procedures appropriate for these brittle materials. The program is specifically concerned with producing high strength, forged alkali halides, alkaline earth halides or simple oxides, and in characterizing the mechanical behavior and developing appropriate design, proof test or inspection techniques for these or other window materials.

Specific areas of research include: a) investigation of the substructure formation during hot forging; b) determination of the effects of additives or impurities on grain boundary mobility; c) investigation into the causes and mechanisms of recrystallization or microstructural instabilities including the inhibiting effects of solutes; d) determination of the effects of forging on mechanical properties to indicate the optimal effects of subgrain and texture hardening and also the strength controlling flaws; e) evaluation of the statistics of macrostrength as influenced by statistical variations in the strength of microstructural elements; f) develop flaw density curves for candidate materials; g) explore various methods of nondestructive evaluation suitable for finding small, sharp cracks of the type expected in brittle materials; h) consider design procedures incorporating statistical predictions, proof testing, and nondestructive evaluation as appropriate.



The work on forging and recrystallization during this reporting period has included forging and microstructural examination of  $\text{CaF}_2$  crystals and further development of the theory on the grain boundary drag in KCl. Crystals of  $\text{CaF}_2$  have been forged and examined by optical microscopy and by transmission electron microscopy. The calculations which showed the effects of an additional strain misfit energy on the interaction potential and the concentration profile between an aliovalent impurity ion and a grain boundary have been extended to show the effect on the impurity drag on the boundary. Finally a simplified analysis has been used to indicate a fluctuation mechanism which can lead to transitions between the low and high velocity modes for a grain boundary.

The crack coalescence fracture model has been modified to include the effects of a free surface and of grain shape on fracture statistics and on the amount of precracking before failure. Techniques for determining actual flaw distribution curves using acoustic emissions and hardness indentation tests have been further elaborated.

The research on this program has been performed by three research groups and has involved a significant contribution from students. Those who have contributed include Professors H. K. Bowen, R. M. Cannon, F. A. McClintock, and J. B. Vander Sande, and research assistants A. M. Glaeser, H. J. Mayson, W. M. Sherry, and M. F. Yan.



## B. MICROSTRUCTURE STUDIES

### B.1. Grain Boundary Mobility in KCl.

#### B.1.1. Strain Field Effect on Impurity Drag

In the previous report, Bowen et al. (1976) theory was presented for the effect of a strain field interaction between an aliovalent impurity and a grain boundary on the space charge potential and the solute and defect concentrations around a boundary. It was shown that if there is a secondary interaction for an aliovalent ion, such as a strain field due to ionic size misfit, it will couple with the electrostatic forces acting on the ion. Near the isoelectric temperature appreciable modification of the segregation expected from purely electrostatic interactions can occur and appreciable electrical fields can be developed near the boundary.

During this period theory has been extended to include calculations of the impurity drag effect on grain boundary mobility for these coupled interaction forces. For these calculations the strain field has been assumed to have the form:

$$U = \begin{cases} U_0 (1 - (x/2a)^n) & x \leq 2a \\ 0 & x > 2a \end{cases} \quad (1)$$

where  $a$  is the lattice parameter,  $n$  determines the rate of decrease of the strain interaction energy in moving away from the boundary a distance  $x$ . The maximum interaction force  $U_0$  is calculated from the elastic strain energy for a sphere with



a radius difference  $\Delta r$  compared to the host ion:

$$U_o = -\frac{4\pi E r^3}{(1+\nu)} \left(\frac{\Delta r}{r}\right)^2 \quad (2)$$

where  $E$  is the elastic modulus, and  $\nu$  is Poisson's ratio. Using typical values for KCl with a  $\text{Ca}^{+2}$ ,  $\text{Sr}^{+2}$ , or  $\text{Ba}^{+2}$  dopant gives values of  $U_o$  of -0.2, -0.05, and  $-10^{-4}$  eV respectively.

Grain boundary velocities have been calculated using the theory and calculation procedures previously described, Yan et al (1975). Values for  $U_o$  of  $\pm 0.2$  and  $\pm 0.05$  eV have been examined for completeness although the strain interaction is expected to be attractive for which  $U_o < 0$ . Most calculations have been done using  $n=1$ , but a few have been done for  $n=2$ . A typical set of results, shown in Fig. 1, for  $U_o = -0.05$  corresponds to an  $\text{Sr}^{2+}$  dopant. The results for  $n=1$  and  $n=2$  are both shown. These can be compared with the previous calculations for the purely electrostatic interaction, Yan et al (1975a), in Fig. 2. The experimental data for similar Sr concentration, 50 ppm, and driving force are also shown.

It can be seen that away from the isoelectric temperature, the effect of the coupled strain field is relatively small. But near the isoelectric temperature the calculated mobility is substantially modified. For the assumed value of  $n=1$ , the general shape of the curves is similar. There is a region in which the driving force exceeds the drag force so that the



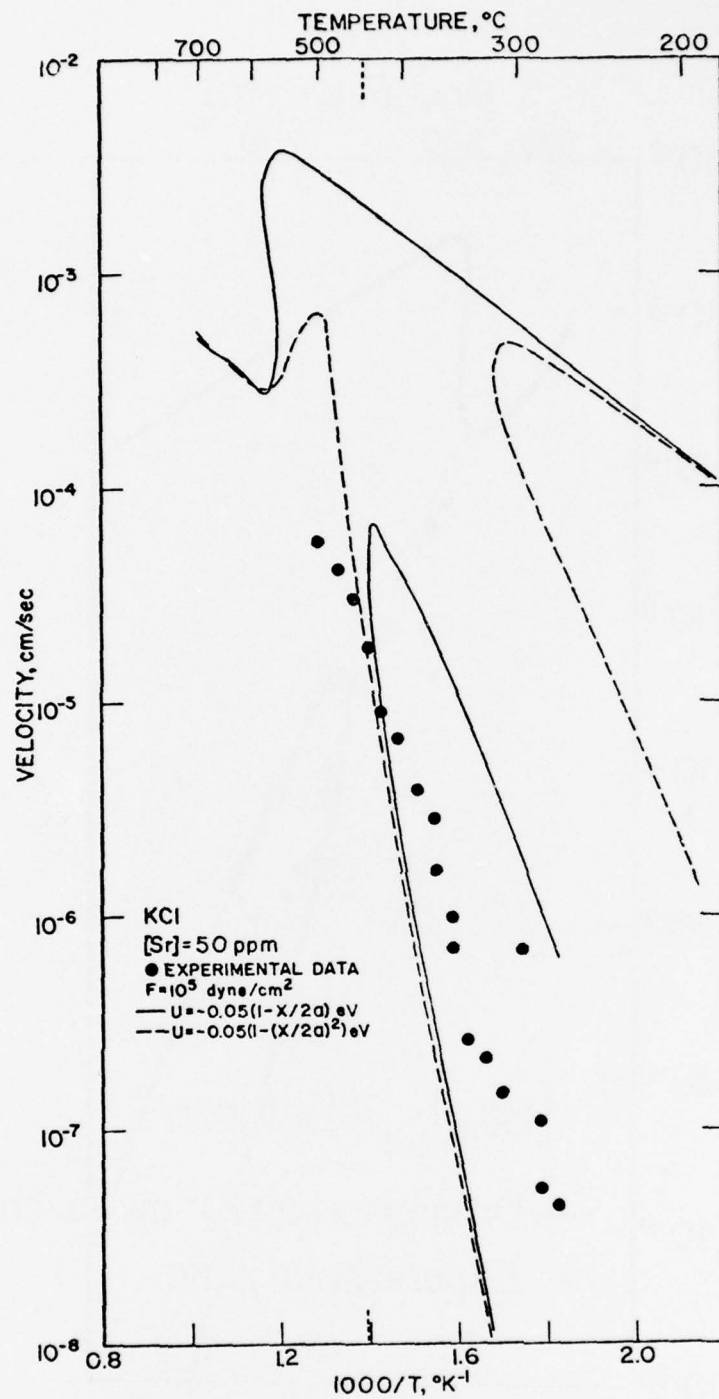


Figure 1: Calculated grain boundary mobility for Sr doped KCl where a strain field interaction force is included in addition to the electrostatic effects.



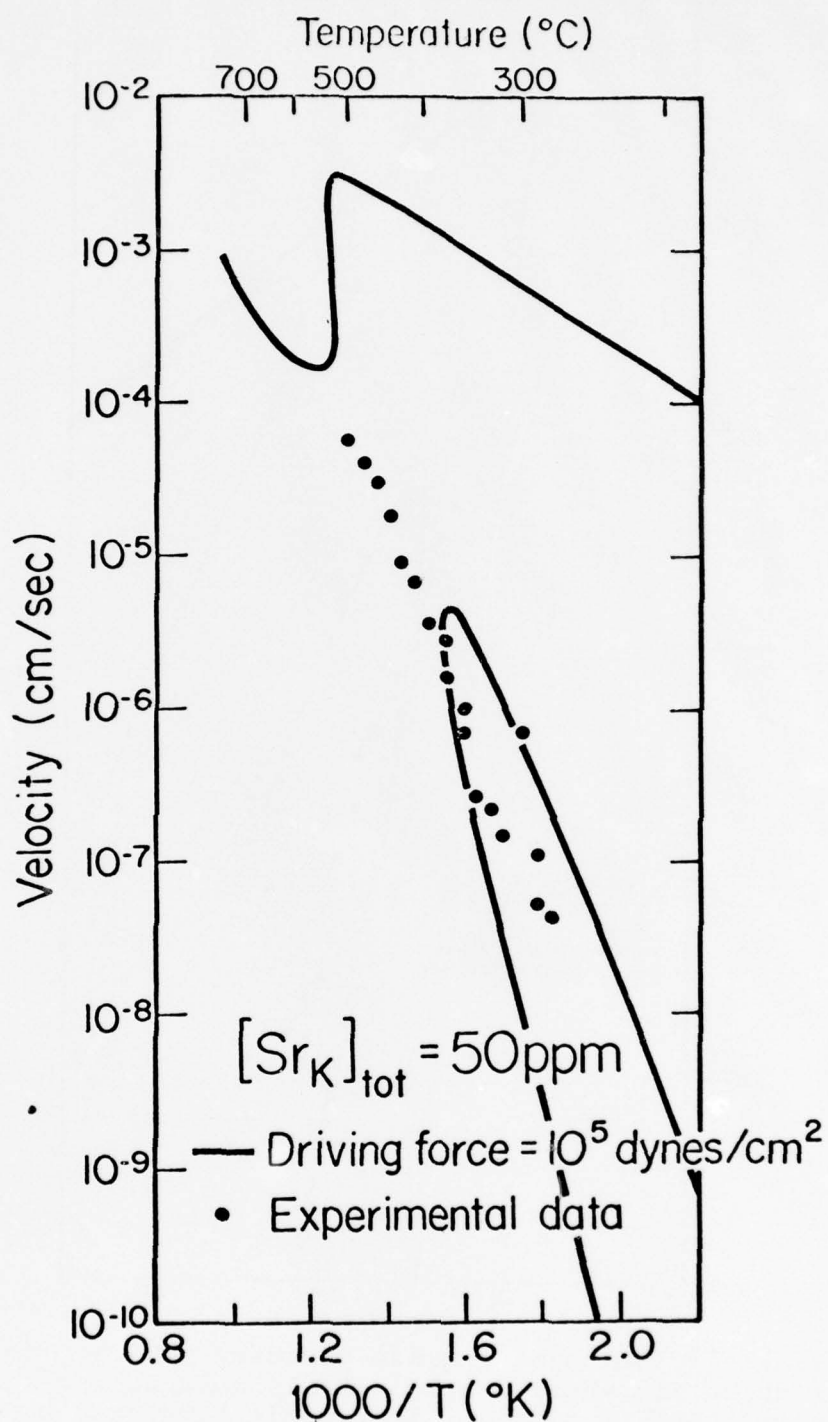


Figure 2: Calculated grain boundary mobility for Sr doped KCl considering only electrostatic interactions.



boundary would move at the intrinsic velocity in this temperature range. For the purely electrostatic interaction, the temperature range for this high velocity behavior is centered about the isoelectric. For the coupled case with  $n=1$ , the temperature range for a single high velocity solution is smaller and further it is displaced to a higher temperature range rather than being centered around the isoelectric temperature. If a repulsive force,  $U_0 > 0$ , is used the gap in the low velocity drag curves shifts to lower temperatures and is centered below the isoelectric. For the  $n=2$  assumption the detailed form of the velocity curve is changed; the cause for this is not presently understood. However for this case the maximum in the velocity is also shifted to a temperature higher than the isoelectric. Where a low velocity solution does exist it is very similar for both assumptions.

The calculations for the coupled strain and electrostatic forces are more approximate than those for the purely electrostatic case because the detailed form of the strain field is not known, but must be approximated and treated parametrically. In addition, the assumption of a negligible velocity dependence of the electrostatic field, which is used in the drag calculation, Yan et al (1975), is not as good for the coupled case as for the purely electrostatic case, especially at high velocities. Nevertheless, the calculations indicate that the low velocity drag is relatively insensitive to the detailed form of the strain



field assumed. Further, the agreement between the experimental data and the theoretical calculations is improved by including a strain field interaction. This suggests the basic concept is valid and warrants further development of the theory. The calculations done to date all suggest that the temperature range for which the impurity drag would be effective would increase in order for the additives  $\text{Ba}^{2+}$ ,  $\text{Sr}^{2+}$  and  $\text{Ca}^{2+}$ .

#### B.1.2. Breakaway from Impurity Cloud

Although the steady state solution for the impurity drag shows that over a range of driving forces either of two stable velocities may occur, the time dependent problem which would indicate the conditions for achieving either mode has not been solved. It is anticipated that transitions between the two modes may result from local fluctuations along the boundary. If the amount of solute at the boundary is reduced it may lead to a transition from the slow to the high speed mode. Conversely, if a region of high speed boundary slows down it may accumulate impurity and then shift to the slow velocity mode. An estimate of the conditions for this instability can be obtained from consideration of the geometrical instabilities which can result during the motion of a planar boundary.

If a boundary has a waviness, as in Fig. 3, the local motion of an impurity as it is dragged by the boundary will include a component perpendicular to the average direction of motion of the boundary. This lead to a tendency to accumulate impurity in the slower regions of the boundary which increases



the drag and may further slow such regions. This convective effect similarly tends to remove impurity from the more rapid, bulging regions leading to a local reduction in the drag. The impurity redistribution (parallel to the boundary) is resisted by parallel diffusion of the impurity and the surface tension of the boundary,  $\gamma$ . From a simplified model of the problem Roy and Bauer (1975) showed that for small fluctuations along a boundary, the position of the boundary and the impurity at the boundary can be expressed in terms of the steady state values for the average velocity,  $V_0$ , plus the correction terms of the form:

$$\Delta X(y,t) = [A_1 \exp(q^+ t) + A_2 \exp(q^- t)] \cos \frac{2\pi y}{\lambda} \quad (3)$$

and

$$\Delta C = [A_3 \exp(q^+ t) + A_4 \exp(q^- t)] \cos \frac{2\pi y}{\lambda} \quad (4)$$

For long wavelengths,  $\lambda$ , at which  $q > 0$ , any fluctuations are stable and will grow spontaneously. By modifying the perturbation analysis to include the nonlinear drag force the condition for instability can be shown to be:

$$\lambda^2 > \lambda_c^2 = \frac{(2\pi)^2 \alpha C_\infty \gamma D'}{F^2 (1 + \beta^2 V_0^2)} \quad (5)$$

where  $D'$  is the effective diffusivity parallel to the boundary.

For all driving forces,  $F$ , if  $\lambda > \lambda_c$  dimensional instability of boundaries can result leading to wavy boundaries. Further,



if  $P_{\min} < F < P_{\max}$ , this geometrical instability may lead to perturbations which allow the transition between velocity modes. ( $P_{\max}$  and  $P_{\min}$  are the maximum and minimum drag forces found in the characteristic impurity drag curve, e.g., Yan et al (1975).) The explicit inclusion of the possibility of evaporation or condensation of impurity from the boundary is expected to lead to a wider range of instability, i.e., smaller  $\lambda_c$ . If a half wave segment shifts from the low to high velocity regime, it may spread laterally and carry a large segment of the entire boundary into the high velocity mode. It is thought that for these intermediate driving forces, the actual velocities of boundaries may be distinctly nonuniform or jerky as they switch from one mode to the other.

## B.2. Hot Forging $\text{CaF}_2$

### B.2.1. Forging

Additional single crystals of  $\text{CaF}_2$  have been forged in vacuo with a graphite die using essentially the same procedures as reported previously, Bowen et al (1976), except that some samples were cooled slowly. Examination of the forged samples by optical microscopy has been done to determine subgrain formation, extent of recrystallization, and the cause of discoloration of crystals forged at high temperatures. The crystals had various random orientations relative to the forging direction. Initial height to diameter ratios were about one and they were forged to 50 to 60% true strain.

The samples all appeared to reach a steady state forging



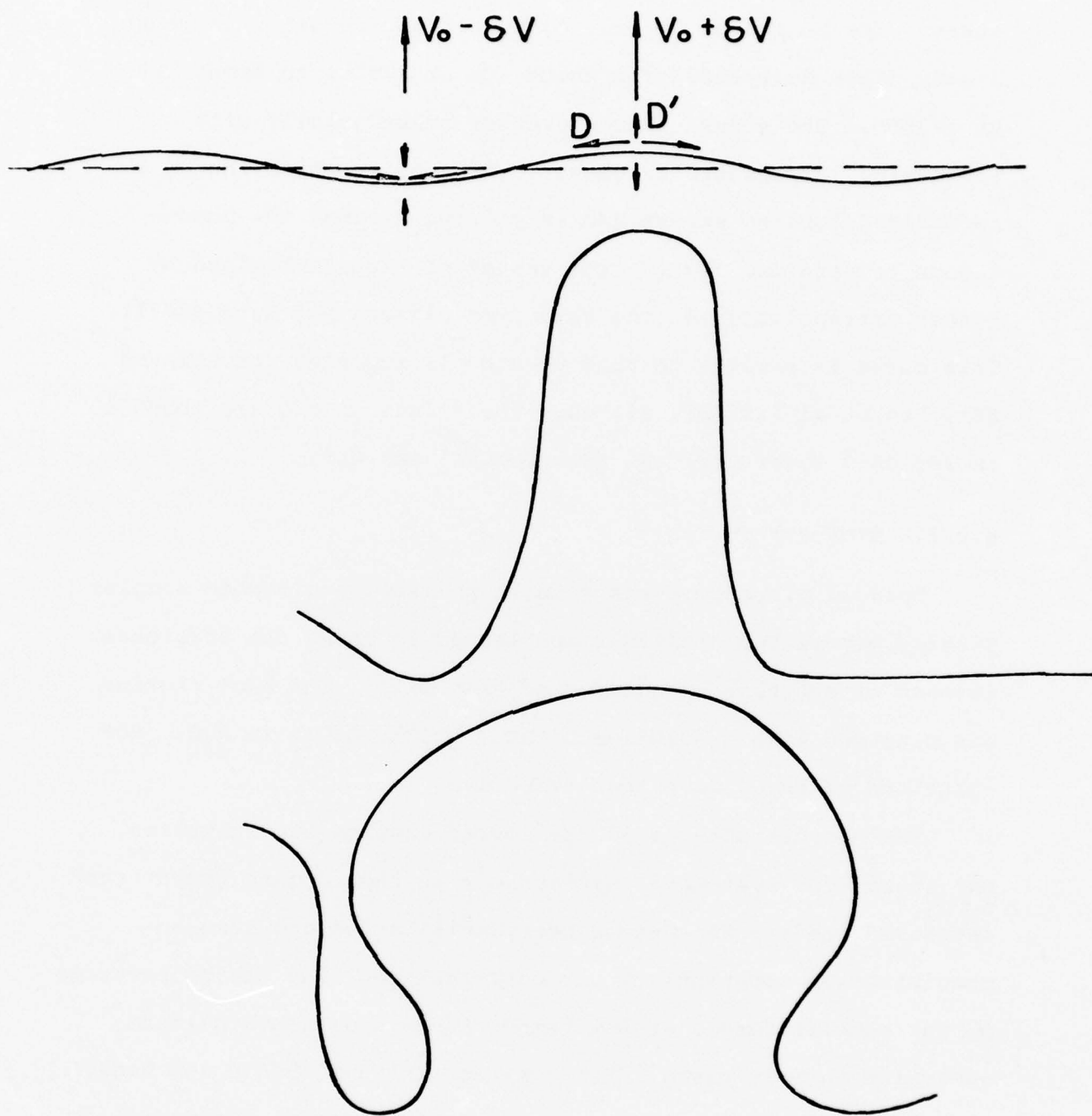


Figure 3: Schematic of breakaway of a grain boundary from its impurity cloud by growth of unstable velocity perturbations.



stress. As indicated in Fig. 4, the strain required to reach steady state decreased from about 40% at 475°C, to about 10% at 1230°C. The stress also decreased substantially with increasing temperature as shown in Fig. 5, in which the normalized forging stress,  $\sigma/E$ , is plotted against the homologous temperature,  $T/T_m$ . The values of  $E$  were obtained by linear extrapolation of the data from Simmons and Wang (1971). This curve is similar to that previously reported for KCl and KBr, Yan et al (1975b), although the values of  $\sigma/E$  are about a factor of 3 lower for  $\text{CaF}_2$  than for KCl and KBr.

#### B.2.2. Microstructures

Optical microscopy was done on polished and etched samples. Etching was rather difficult and tended to bring out scratches instead of subgrain boundaries or etch pits. The best etching was obtained with a solution of HCl,  $\text{NH}_4\text{Cl}$ ,  $\text{AlCl}_3$  in  $\text{H}_2\text{O}$ . Hot solutions of  $\text{NH}_4\text{Cl}$  were less effective.

The microstructures of the forged samples had subgrains, but there were systematic differences as the forging temperature increased leading to dynamic recrystallization and also to precipitation apparently from contamination. The microstructures of the samples forged at low temperatures had rather uniform subgrains in most cases. For samples forged at 900°C and higher the sample interiors were nearly free of subgrains apparently as a result of dynamic recrystallization; patches of subgrains were typically evident around the edges of these samples. The micro-



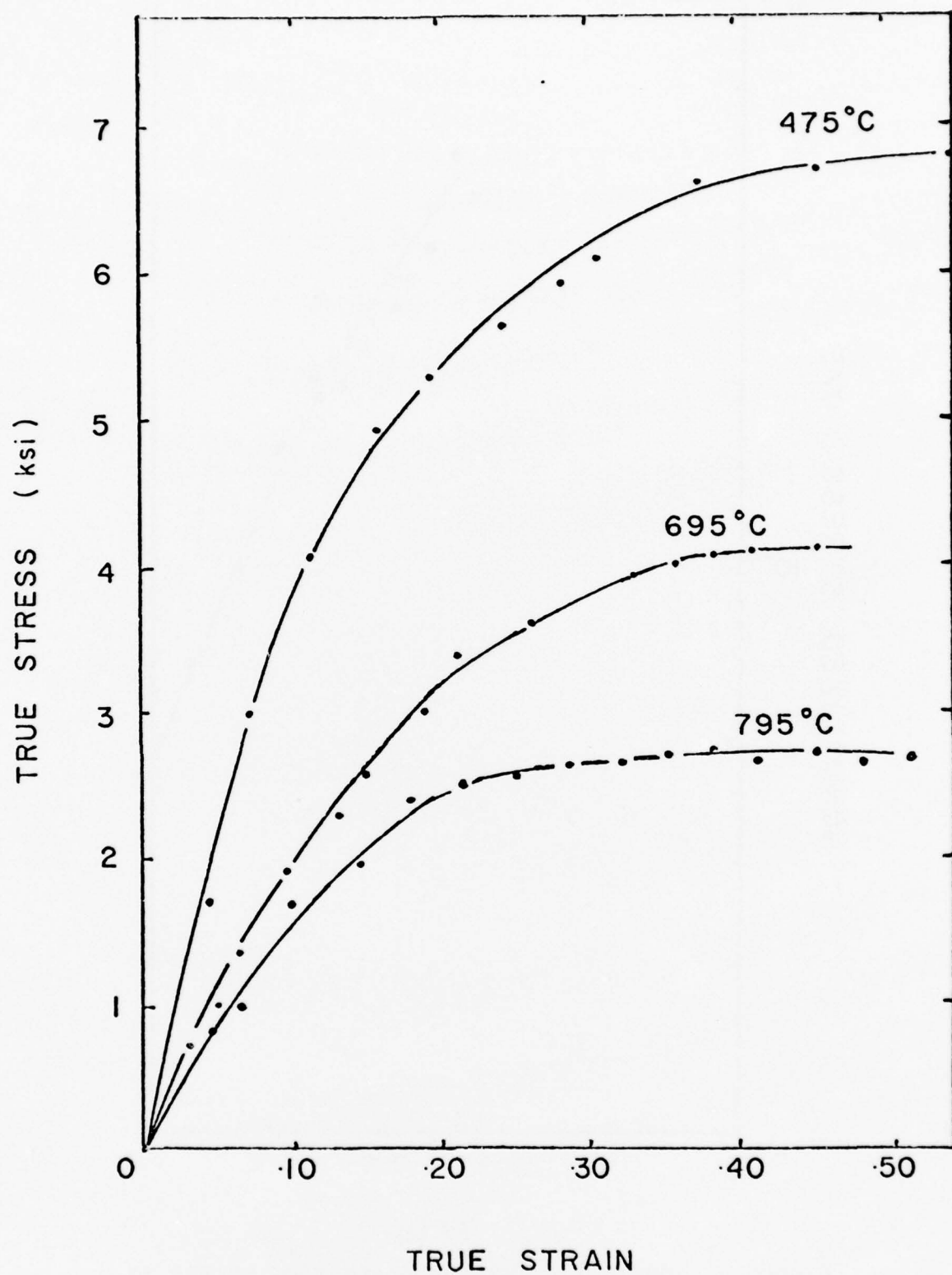


Figure 4: Representative stress-strain curves for forged  $\text{CaF}_2$ .



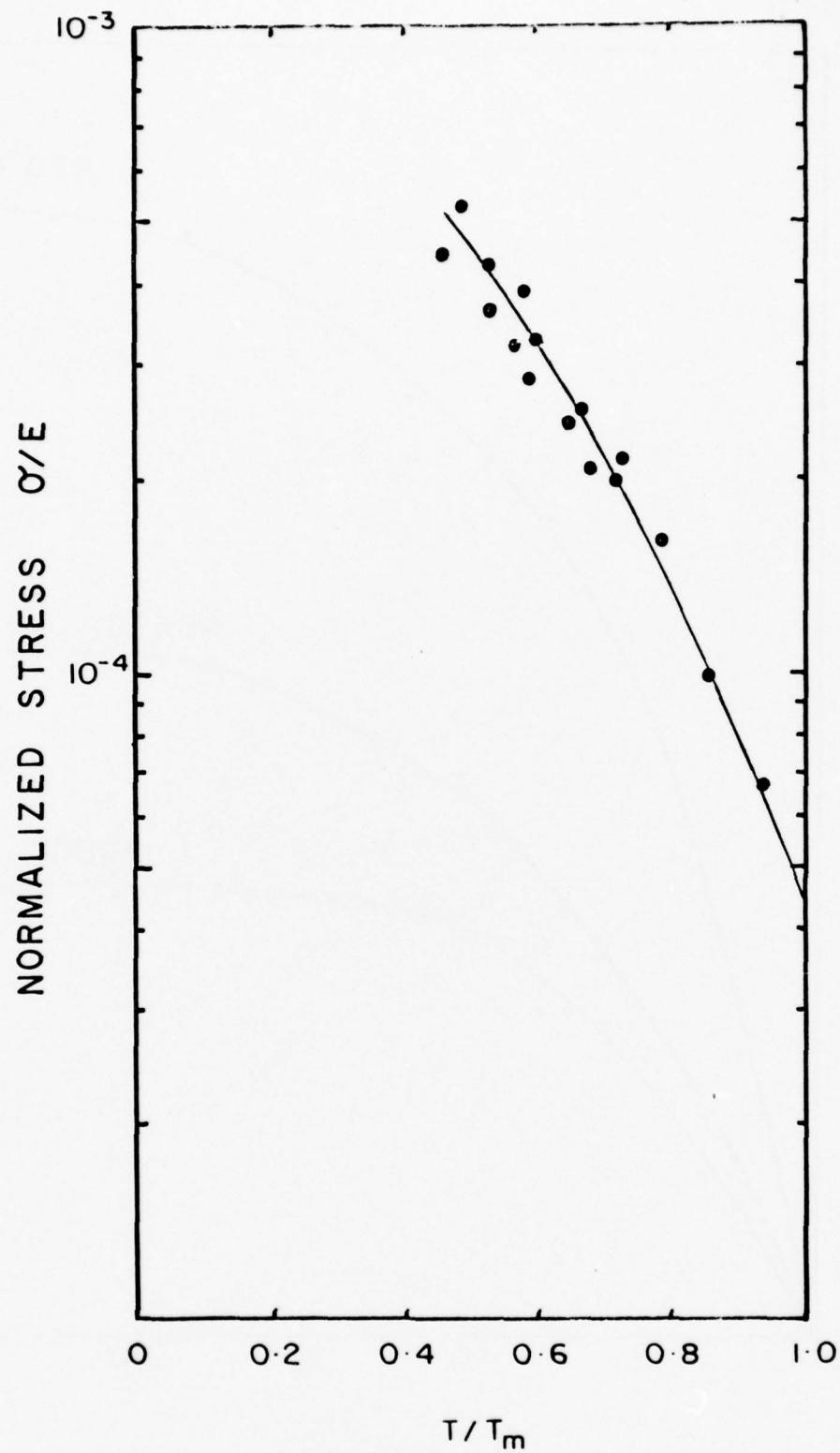


Figure 5: Normalized steady state flow stress as a function of temperature for  $\text{CaF}_2$  forgings.



structures of the slow cooled and the quenched samples had similar features.

The subgrain structures found are similar to those previously reported in the forged KCl and KBr and to the creep substructures observed in many metals. A typical microstructure is shown in Fig. 6. For the samples forged below 600°C the boundaries did not etch as sharply. This was particularly evident in the 475°C sample, Fig. 7, in which a cellular structure is seen. The lack of sharply etched boundaries suggests they are still dislocation tangles and not sharply knit sub-boundaries. There was a tendency for the grains to be elongated in some samples as shown in Fig. 8, taken from a sample forged at 695°C. In some samples dislocation cells within the grains were clearly evident, Fig. 9. The subgrain boundaries are all low angle boundaries, but the boundaries of the inner cells have even lower misorientation angles.

In samples forged at higher temperature there were frequently large regions in which there were either no subgrains, or if they were present they etched very lightly. In samples forged at 900 to 1000°C well defined subgrains were only found in the region around the surface of the sample as shown in Fig. 10a). The lightly etched subgrains in the sample interior are shown in Fig. 10b. This is thought to result from dynamic recrystallization during forging. The time between recrystallizations is so short that the subgrain boundaries do not survive for enough strain to reach a misorientation angle typical of





Figure 6. Subgrain structure in  $\text{CaF}_2$  forged at  $795^\circ\text{C}$ .



Figure 7. Subgrain structure in  $\text{CaF}_2$  forged at  $475^\circ\text{C}$ .



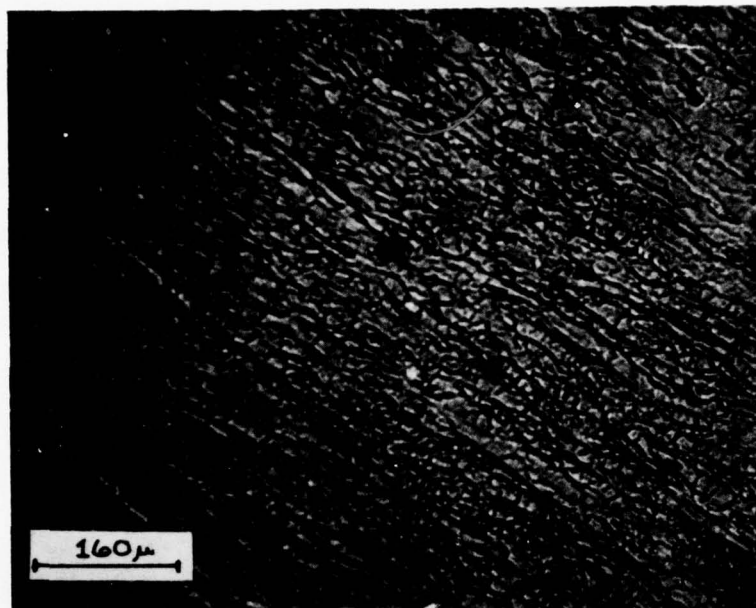


Figure 8. Elongated subgrains in  $\text{CaF}_2$  sample forged at 695°C.

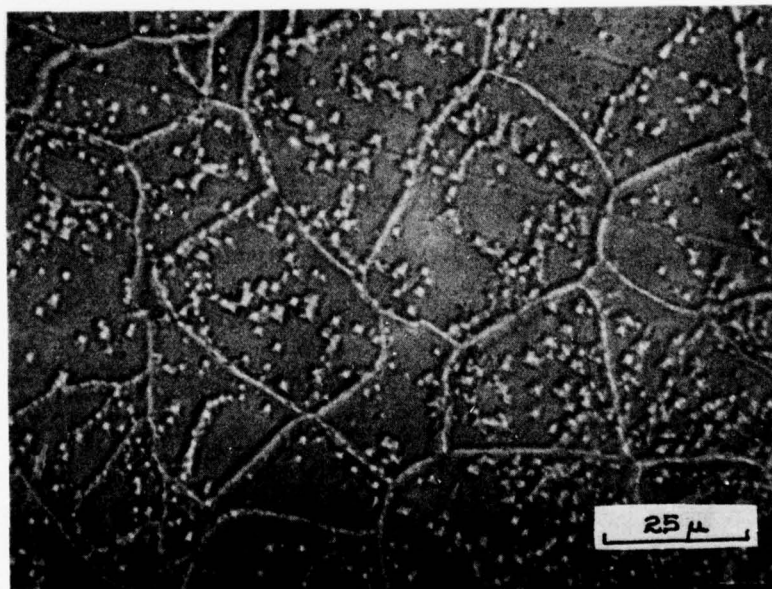


Figure 9. Dislocation cells within subgrains in  $\text{CaF}_2$  specimen forged at 795°C.



steady state creep. A new grain with an incompletely developed subgrains is shown in Fig. 10c. There was evidence of dynamic recrystallization in some samples at temperatures as low as 580°C ( $0.49T_m$ ). Similar behavior has been seen in KCl or KBr, but it was not seen at temperatures below  $0.8 T_m$  in pure specimens and it was restricted to even higher temperatures in doped samples, Yan et al (1975b). The results to date indicate that recrystallization is a much more serious problem in  $\text{CaF}_2$  than in KCl or KBr.

Samples forged at 1120 and 1230°C were cloudy or opaque after forging. Plate like precipitates were found in these samples after forging. They have not been identified, although it is thought likely that they are caused by oxide contamination.

The subgrain size was found to vary inversely with the forging stress. The measured subgrain size (mean linear intercept) is plotted against the forging stress in Fig. 11. The results are qualitatively similar to those for KBr and KCl, which are also shown, but the slope is much steeper than typically expected. The plot does not include data for samples forged at 1100°C and above which suffered contamination problems and had few regions with subgrains.

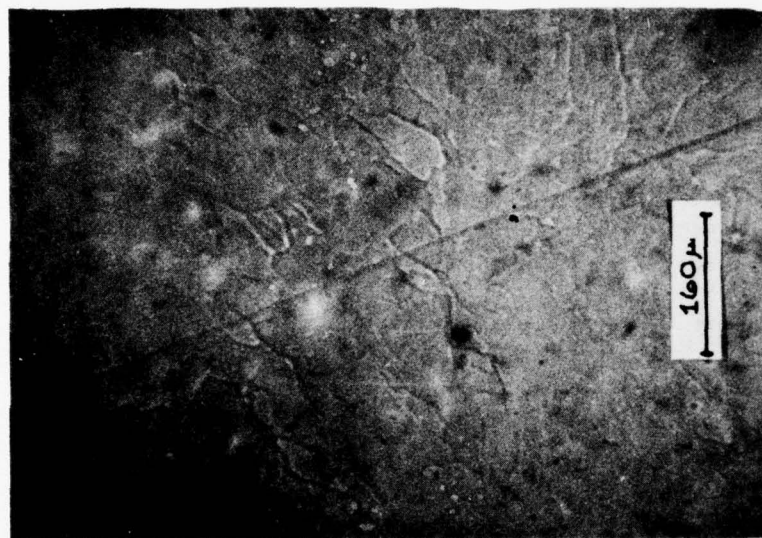
### B.3. Transmission Electron Microscopy of Hot Forged $\text{CaF}_2$

In an effort to quantitatively analyze the microstructure of  $\text{CaF}_2$ , transmission electron microscopy has been initiated. The need for this quantitative analysis of the microstructure is

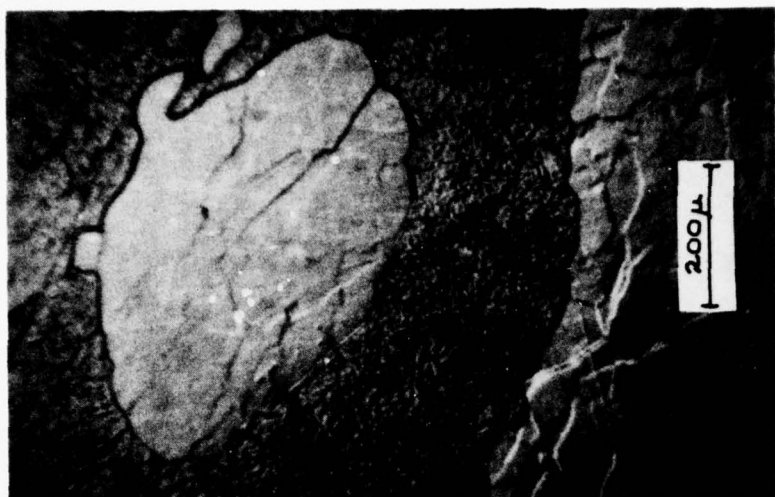




a)



b)



c)

Figure 10. Microstructure near edge (a) and in center (b) of sample forged at 1018°C. A partially recrystallized region (c) is shown in which there is a new grain with incompletely developed subgrains within it caused by dynamic recrystallization during forging.



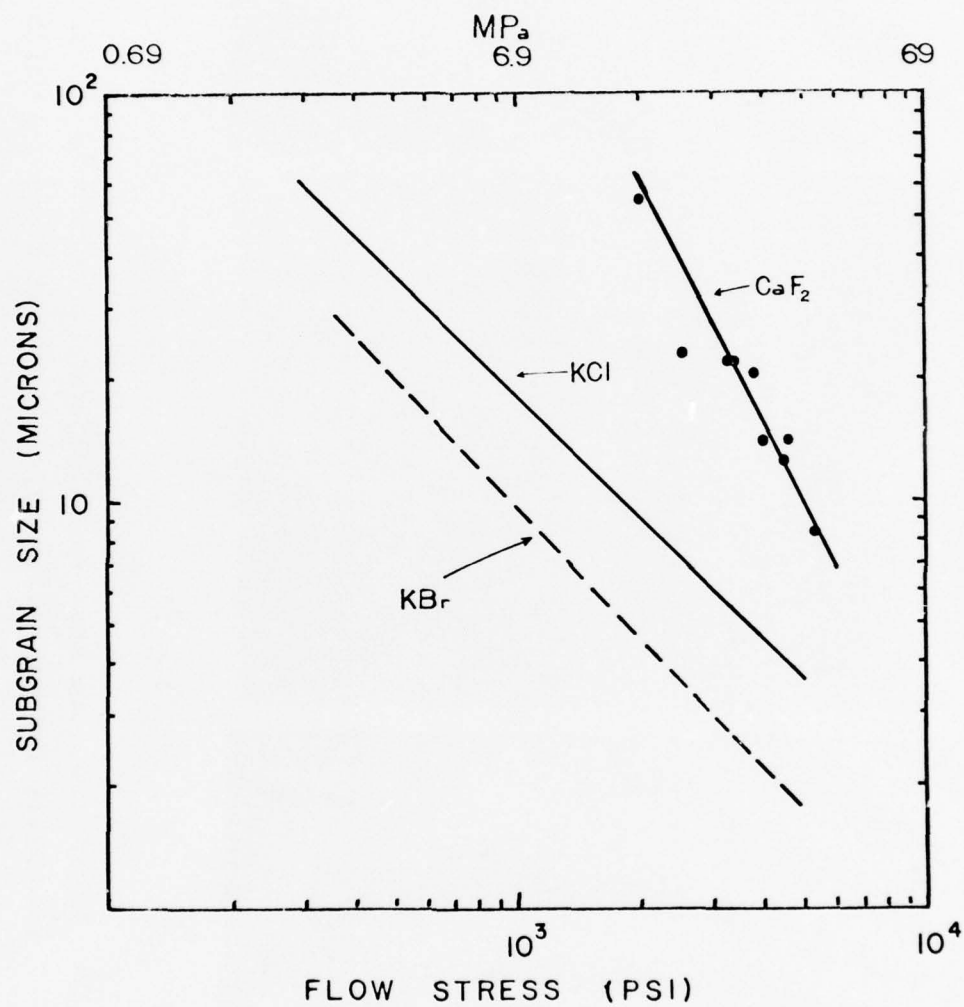


Figure 11: Subgrain size versus forging stress for CaF<sub>2</sub>. Similar curves for KCl and KBr, Yan et al. (1975a) are shown for comparison.



twofold: first, it combines with the deformation schedule to provide structure/mechanical property data; and, second, the microscopy provides data on many of the physical parameters that are important in the recrystallization theory developed under this program.

This section of this report describes the experimental procedure for the successful electron microscopy of  $\text{CaF}_2$  and some preliminary results on the microstructure of hot forged  $\text{CaF}_2$ . Additional results are forthcoming, with the aim of providing sufficient observations to yield statistically meaningful conclusions.

#### B.3.1. Experimental Procedure

Hot forged  $\text{CaF}_2$  specimens were cut to approximately  $500\mu$  thick slices using a string saw with a cutting solution of SiC powder, glycerin, and water and a string saw wire diameter of  $375\mu\text{m}$ . The  $500\mu\text{m}$  thick specimens were then mounted on a polishing jig using a low melting point wax and polished on 500 grit emery paper to approximately  $375\mu\text{m}$  in thickness. The slices of  $\text{CaF}_2$  were next cut, using either the string saw or a surgical blade, to fit into a 3 mm specimen holder. The specimens were then chemically jet thinned for transmission electron microscopy.

Chemically jet thinning  $\text{CaF}_2$  for transmission electron microscopy is difficult for two reasons. First, because  $\text{CaF}_2$



is luminescent, conventional means for detecting the appearance of a hole in a specimen during the jet thinning process cannot be employed. Secondly,  $\text{CaF}_2$  polishes (etches) nonuniformly.

Several solutions have been tried as possible candidates for the jet chemical thinning process; these are listed in Table I. The chemical solution which has yielded the most uniform polish is: 400 ml  $\text{H}_2\text{O}$ , 100 ml  $\text{HCl}$ , 70 gm  $\text{AlCl}_3$ , and 70 gm  $\text{NH}_4\text{Cl}$ , at  $70^\circ\text{C}$ .

Thin foils are made using a dual jet thinner. The specimen is observed during thinning with a light microscopy using transmitted light to illuminate it. When the light is properly aligned, and reflected light is used to observe the specimen, fine structure on the surface of the specimen may be observed. A hole is generally not observable until it is 0.5 to 1 mm in diameter, resulting in a major portion of the thin area being lost, which makes the transmission electron microscopy more difficult.

Before a specimen is placed in the electron microscope, it is coated with a thin layer of carbon to prevent specimen charging. The carbon is applied by vapor deposition.

#### B.3.2. Results

Initial transmission microscopy was done with the specimen at room temperature. Due to excessive irradiation damage from the electron beam any microstructural features were obliterated. Subsequent observations in the electron microscope were performed using a cold stage operating with liquid nitrogen as a coolant



TABLE I

Chemical Polishing Solutions for  $\text{CaF}_2$ : Jet ThinningA.  $\text{NH}_4\text{Cl} + \text{H}_2\text{O}$ 

<u>Concentration</u> (gm/100 cc $\text{H}_2\text{O}$ )	<u>Temperature</u> (°C)	<u>Time</u> (min)	<u>Remarks</u>
1.34	22	100	
2.67	22	100	No visible change in specimen
5.35	22	100	
8.87	22	100	
8.00	18	60	No visible change in specimen
	40	60	
20.0	40	30	No visible change in specimen
	60	30	
	80	30	
	90	30	
20.0	~20	5700	No visible change in specimen

B.  $\text{CH}_3\text{COOH}$ 

<u>Normality</u> N	<u>Temperature</u> (°C)	<u>Time</u> (min)	<u>Remarks</u>
.8	20	5700	No visible change in specimen

C.  $\text{NH}_4\text{OH} + \text{H}_2\text{O}$ 

<u>Concentration</u> (ml $\text{NH}_4\text{OH}$ /100 ml $\text{H}_2\text{O}$ )	<u>Temperature</u> (°C)	<u>Time</u> (min)	<u>Remarks</u>
10	21	45	No weight loss
50	21	45	
∞	21	45	



Table I (continued)

D.  $\text{HF} + \text{H}_2\text{O}$ 

<u>Concentration</u> (ml HF/100 ml $\text{H}_2\text{O}$ )	<u>Temperature</u> (°C)	<u>Time</u> (min)	<u>Remarks</u>
1	21	35	No weight loss
2	21	36	No weight loss
4	21	39	No weight loss
10	21	41	No weight loss
20	21	38	5% weight loss
30	21	35	5% weight loss
$\infty$	21	50	12% weight loss

E.  $\text{NH}_4\text{Cl} - \text{AlCl}_3 - \text{H}_2\text{O}$ 

<u>Concentration</u>	<u>Temperature</u> (°C)	<u>Time</u> (min)	<u>Remarks</u>
20 gm $\text{NH}_4\text{Cl}$			
20 gm $\text{AlCl}_3$	70	30	25% weight loss
200 ml $\text{H}_2\text{O}$			



which greatly reduced the irradiation damage; however, specimen contamination became a minor problem.

Representative micrographs of  $\text{CaF}_2$  hot forged at  $1229^\circ\text{C}$  as observed at room temperature and at approximately  $-120^\circ\text{C}$  are presented in Figs. 12a and 12b, respectively. The effects of the electron beam on the microstructure of the room temperature observation is clearly evident. High densities of point defects have been generated due to irradiation damage from the beam. The point defects appear to form in rows along  $\langle 220 \rangle$  and  $\langle 422 \rangle$  directions leading to a pronounced texture in the sample. This array of point defects is the final stage of the irradiation damage process. However, due to the cryogenic temperatures employed during TEM, the specimen contaminates. Provided the microscope is as "clean" as possible before commencing, specimen contamination is minimized. The contamination generally appears as black spots and obscures the background structure.

Results of transmission electron microscopy observations at  $-120^\circ\text{C}$  of  $\text{CaF}_2$  hot forged at  $590$ ,  $817$ ,  $1109$ , and  $1229^\circ\text{C}$  are presented in Figs. 13-16. The effects of forging temperature on dislocation density and subgrain boundary structure can be seen. For the lowest forging temperature,  $590^\circ\text{C}$ , the subgrain boundaries are composed of dislocations which are only occasionally observed to be in an equilibrated structure (Fig. 13b). Often, dislocations can be found in cell interiors (Fig. 13c). Samples forged at  $817^\circ\text{C}$  and  $1109^\circ\text{C}$  exhibit a higher density of equilibrated boundaries (Figs. 14 and 15). Occasional "free" dislocations are, however, still observed in cell interiors. Few boundaries or





(a)

0.5 μ

$\bar{g}$  422



(b)

0.5 μ

Figure 12:  $\text{CaF}_2$  hot forged 1229°C (a) room temperature TEM  
(b) -120°C TEM



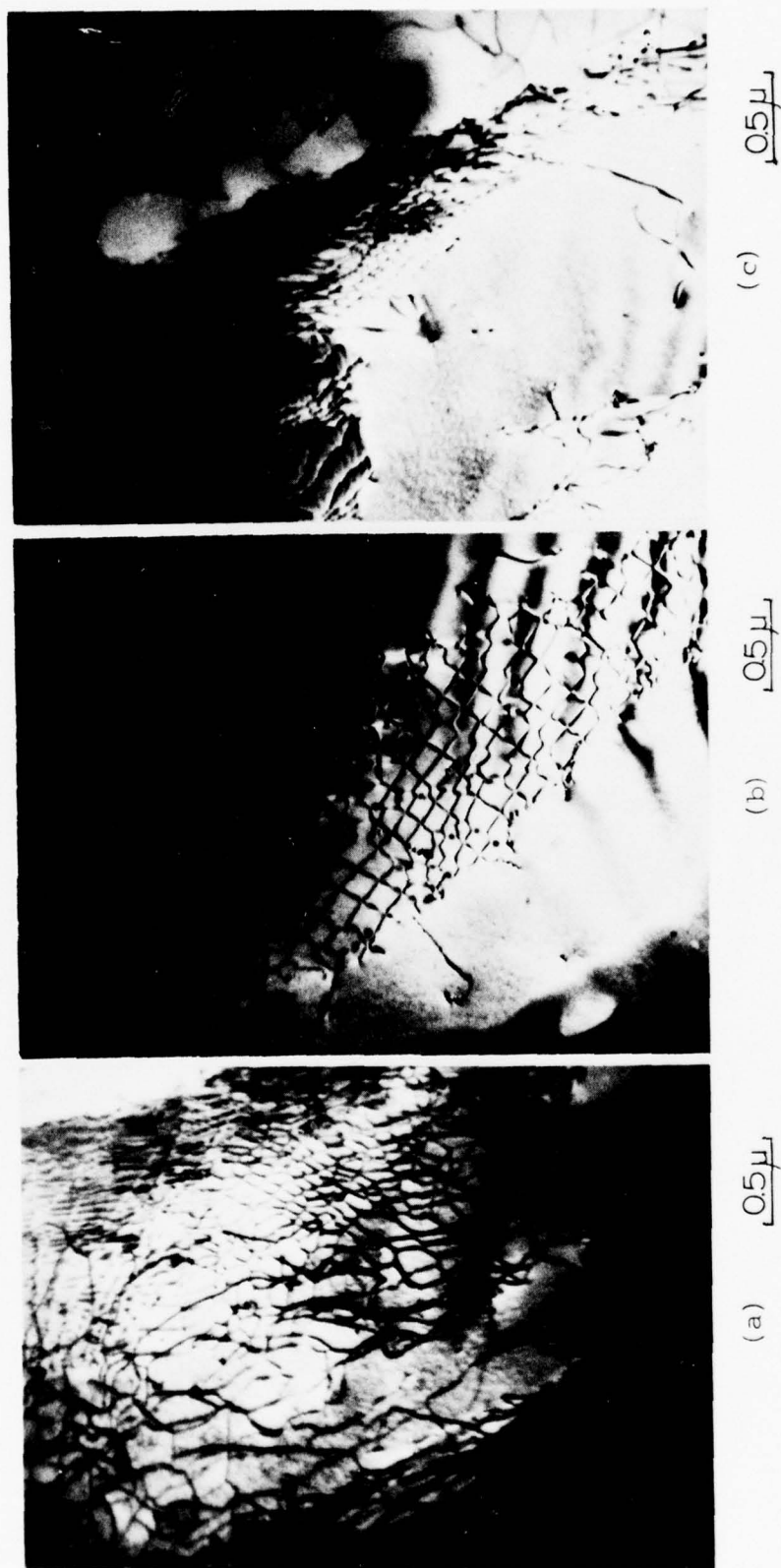


Figure 13:  $\text{CaF}_2$  hot forged  $590^\circ\text{C}$ .



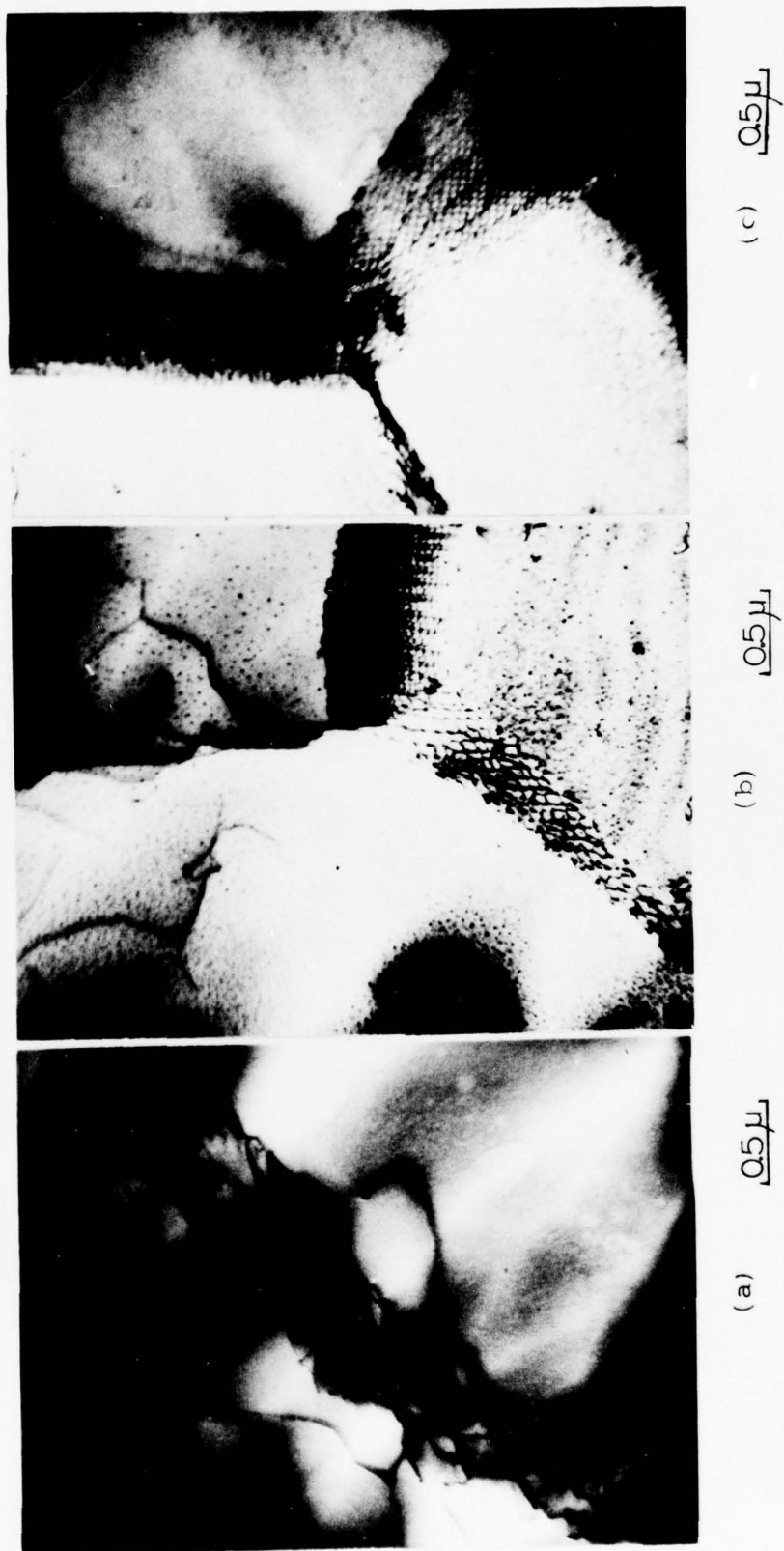
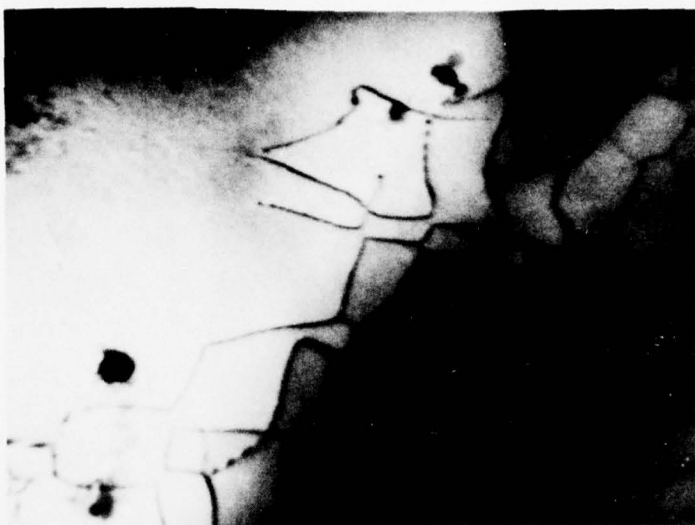


Figure 14:  $\text{CaF}_2$  hot forged  $817^\circ\text{C}$ .





(c)  $0.5\mu$



(b)  $0.5\mu$



(a)  $0.5\mu$

Figure 15:  $\text{CaF}_2$  hot forged  $1109^\circ\text{C}$ .



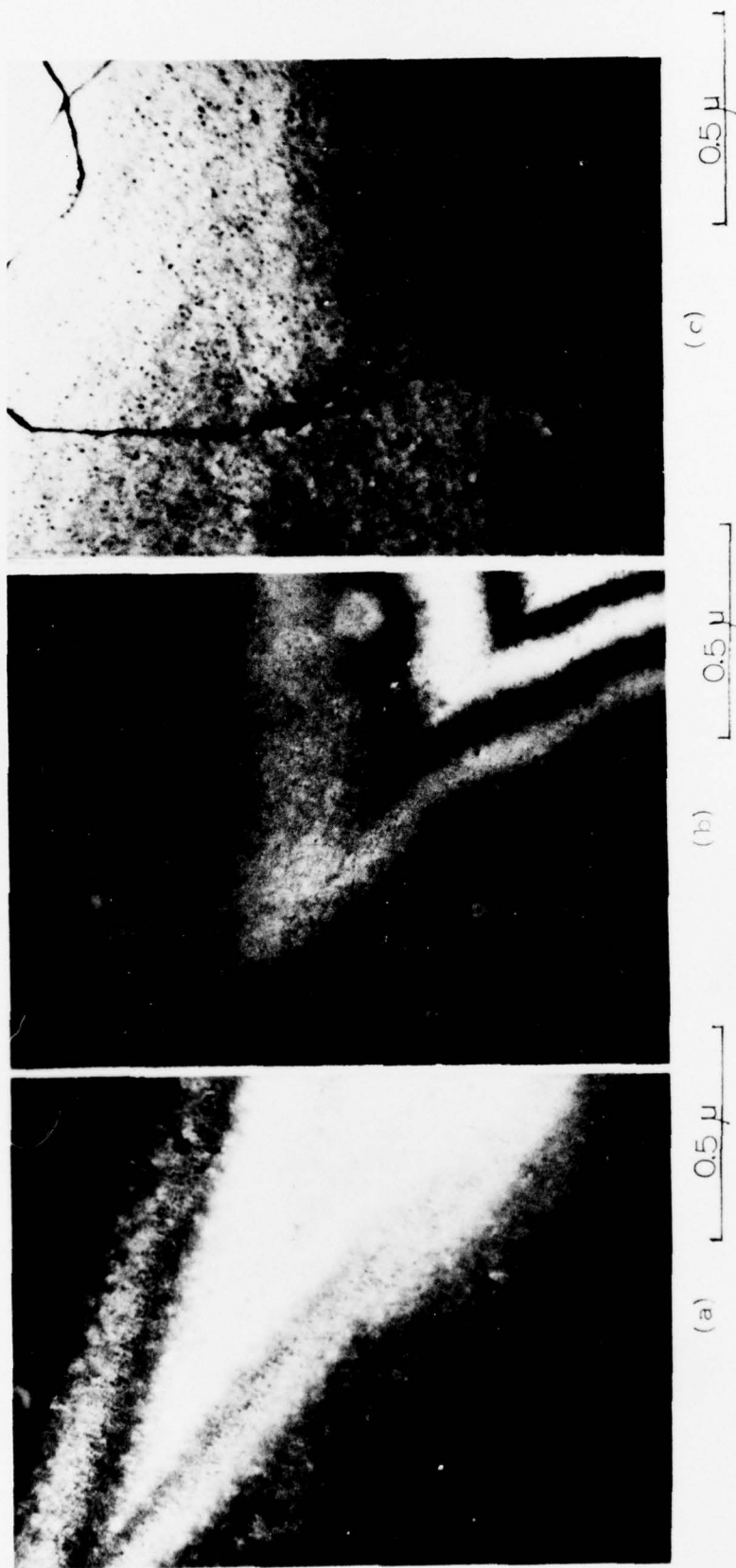


Figure 16:  $\text{CaF}_2$  hot forged  $1229^\circ\text{C}$ .



dislocations are observed when  $\text{CaF}_2$  is forged at  $1229^\circ\text{C}$  (Fig. 16). The lower density sub-boundaries in Figs. 14a and 15c may be similar to the interior cell walls shown in Fig. 9.

### C. FRACTURE OF BRITTLE MATERIALS

The initiation of subcritical microcracks and their subsequent localization to form a microcrack has been studied numerically and analytically by McClintock and Zaverl (1974). The restriction of biaxial loading was relaxed by McClintock and Mayson (1976) to find the effects of changing the applied tensile stress components, while still maintaining enough tension to avoid the effects of crack closure and friction. In each case microcracking and subsequent macrocrack formation was assumed to occur within an infinite medium. Many brittle materials, e.g., zinc solenide (Evans, 1976) have fracture origins not within the bulk but at the surface. The models have been extended here to study the effects on brittle crack statistics of surface or near surface initiated fracture.

Previous work on brittle crack statistics has assumed a two-dimensional array of regular hexagon grains and this restriction has been relaxed to more accurately represent actual brittle materials. A preliminary investigation has been carried out to study the effects of elongated grains on statistical strengths.



Accurate strength distribution curves assist the designer in predicting the behavior of brittle components. They can also give insight into ways in which manufacturing techniques can be altered to improve the ultimate performance of the finished produce. Two methods of obtaining strength distributions from laser window materials and polycrystalline ceramics have been considered. The first enables the statistical parameters that govern the strengths of individual grain boundaries, idealized as an extreme value distribution, to be found from macroscopic acoustic emission data. The second employs a hardness indentation - acoustic pick up approach on a microscopic level.

## C.2. A Model of Surface Brittle Crack Initiation

### C.2.1. Numerical Model.

The numerical model of surface brittle crack initiation is a form of boundary integral method in which crack segments are modelled by dislocation arrays. This is achieved by inserting a relative displacement dart  $D^m$  across the  $m^{th}$  segment. The dart is defined as the Burgers vector at the second end of the segment.

The resulting traction  $t^\mu$  on the  $\mu^{th}$  segment due to the  $m^{th}$  cracked segment is given by the influence coefficient  $T^{\mu m}$ , which is analogous with a Greens function (Hildebrand, 1952), and accounting for the applied stress at infinity  $t^{\infty\mu}$  gives:

$$t^\mu = T^{\mu m} D^m + t^{\infty\mu}$$



The requirement for zero normal and shear stresses at the free surface is satisfied by using the stress field of a near surface dislocation (Head, 1953) to determine tractions and influence coefficients.

All cracked segments are assigned traction free so that the darts must be chosen to cancel the effects of the applied stress. Having solved for all darts, the stress can be found anywhere in the body by superimposing the stress fields of all cracked segments.

The stress is calculated at each grain boundary and the stress intensities are found at each crack tip. The weakest segment relative to its applied stress is found and assumed to be cracked. The calculation is repeated until the externally applied stress reaches a maximum value just prior to macroscopic crack propagation.

The results from the numerical model are discussed after the next section.

#### C.2.2. Analytical Model.

The extension to study surface effects of the analytical formulation of McClintock and Mayson (1976) is straight forward. As before the models estimate the maximum strength by first finding the density of unit cracks as a function of the applied stress. The probability of aggregation of these cracks is estimated. The maximum strength being achieved when crack length and stresses are sufficiently high to cause crack propagation even with median strengths at the crack tip.



The density of unit cracks under a given applied stress and corresponding longest contiguous chain having a median probability of forming are unaffected by the presence of the surface. However, the intensities of any surface cracks are different from those embedded within the material and this has been accounted for.

#### C.2.3. Discussion of Results

Part sizes up to 1000 grain segments were studied using the numerical model. The results are shown in Figs. 17 and 18 for two different variabilities ( $m = 3, 10$ ). The first crack is critical for part sizes longer than the previously considered case of embedded fracture. However, for larger part sizes, the size effect cannot be predicted by extreme value statistics which are only valid when fracture is governed by first cracking (Dukes, 1971).

The maximum strengths as predicted by the analytical models are shown and a drop of 10-20%, depending on orientation and variability, occurs for surface initiated fracture. This relatively small drop would suggest that the statistical treatment of brittle materials is somewhat independent of whether fracture is initiated in the bulk or at the surface of the material as long as the relevant distribution of grain boundary strengths is used. It should be noted that even a drop of 10% in maximum strength can significantly reduce the amount of precursor acoustic emission.



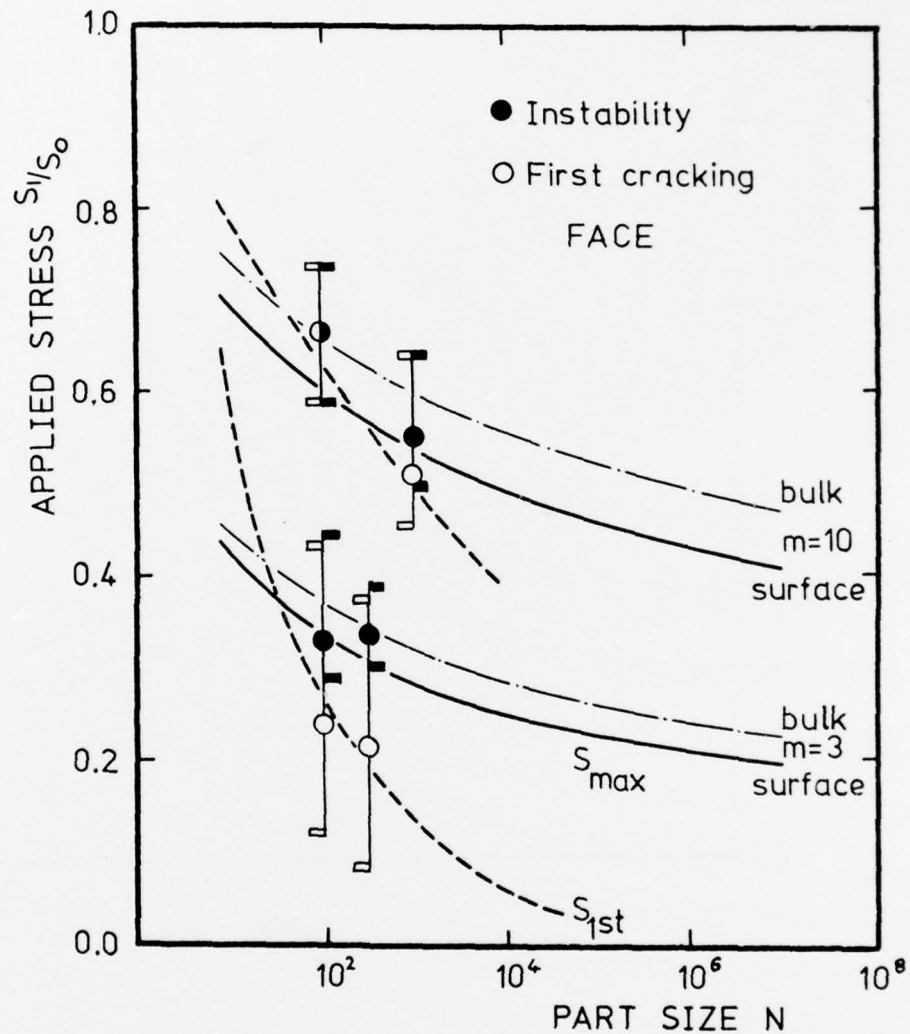


Figure 17: Statistical strength for the face orientation as a function of part size for surface initiated fracture and for comparison the curve for bulk fracture is shown. Strength distributions of  $m=3$  and  $10$  with  $S_L/S_0=0$ . Samples of  $5$ , giving  $93.75\%$  confidence limits for the median.



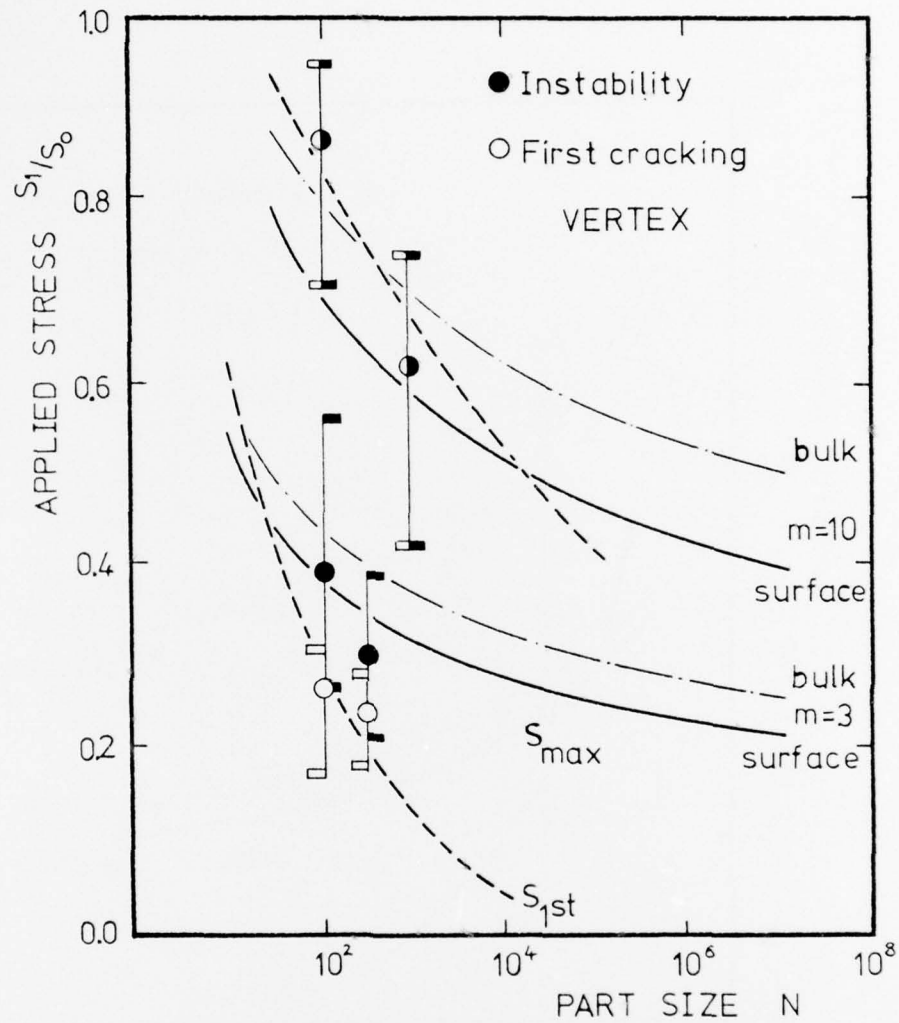


Figure 18: Statistical strength for the vertex orientation as a function of part size for surface initiated fracture and for comparison the curve for bulk fracture is shown. Strength distributions of  $m=3$  and  $10$  with  $S_L/S_0 = 0$ .



### C.3. Statistical Strength and Grain Shape.

Previous work on brittle crack statistics has assumed a two-dimensional array of regular hexagon grains. The computer model of the mechanics and statistics of brittle crack initiation has been used to study the effects of elongated grains on statistical strength. Preliminary results indicate that the maximum strength falls as the slenderness ratio (length to width) of the grains increases, while the first cracking remains constant. This work is being continued and the possibility of incorporating grain boundary strength distributions that also vary with segment length will be considered.

### C.4. Obtaining Strength Distributions From Acoustic Emissions.

#### C.4.1. Acoustic Emission and Brittle Materials.

Acoustic emissions are the stress waves originating from strain energy release as a result of various physical and structural changes within the material caused by the applied stress.

The strain energy released in the formation of micro-cracks, prior to maximum load, observed by Evans (1974), is thought to be the cause of acoustic emission in many polycrystalline ceramics and possibly other materials that exhibit barely any dislocation motion at room temperature. Also, as would be expected, no acoustic emission is observed from amorphous brittle materials, Noone (1973), except at the onset



of catastrophic failure. Others, Graham and Alers (1973), have observed a relationship between detected acoustical events and fractured grains and for Lucalox found a one-to-one correspondence. Noone (1973) in the same material similarly attributed a single acoustical event with the parting of two grain surfaces.

The above strongly suggests that for many brittle materials any detected acoustic emission is due to the formation of stable micro-cracks.

#### C.4.2. Analysis of Experimental Data.

The formation of stable micro-cracks at stresses below the ultimate fracture load suggests a way of obtaining the statistical parameters  $m$ ,  $S_0$  and  $S_1$  that govern the grain boundary strengths idealized as an extreme value distribution of the third kind.

These parameters may be found from macroscopic acoustic emission data taken in the form of "count rate" against applied stress for tests conducted at constant stress rate. There is only a limited amount of suitable data available in the literature and all of it for polycrystalline ceramics. For example the data of Evans (1974) gives a value for the exponent  $m$  of about 8 for unpolished specimens Lucalox. The effect of polishing was to significantly reduce the amount of acoustic activity as well as increasing  $m$  to about 25. This suggests that many of the low strength grains, damaged during



manufacturing and machining have been removed from the surface by polishing. Removal of the low strength grains during polishing would account for the low acoustic activity from optically finished samples of zinc selenide as observed by Evans (1976).

#### C.5. Flaw Density Distributions from Indentation Tests.

The flaw density distributions of brittle materials can be obtained from many different kinds of tests often with varying stress fields. Argon (1959) obtained such distributions from an extensive series of indentation tests on various glasses. Mathews (1976) developed a more generalized procedure of analyzing such data. Such tests carried out on a small scale have the advantage of yielding large amounts from samples of a limited size. It should be noted that meaningful distributions are obtained only if test specimens have been treated and polished to the same specifications as required for large scale components.

The difficulty in using indentation or similar tests is in readily detecting the cracks formed. Moreover many laser window materials and polycrystalline ceramics are opaque to visible light and optical techniques could not be employed. One possibility would be to use two or three acoustical pickups placed around the indenter to monitor the sample while it's under load. It is felt that such a technique could also provide further insight into the relationship between detected acoustical events and micro-cracking.



#### D. REFERENCES

- Argon, A. S., (1959) "Surface Cracks on Glass", Proc. of Royal Society, A, 250, 442.
- Argon, A. S. (1959), "Distribution of Cracks on Glass Surfaces", Proc. of Royal Society, 250, 482.
- Bowen, H. K., et al (1976), Research on Materials for High Power Laser Window, ARPA Contract F19628-75-C-0191, Semi-Annual Technical Report, for the period ending 31, November, 1975.
- Dukes, W. H., (1971), Handbook of Brittle Material Design Technology, ARGARD-AG-152-71, pp. 1-16.
- Evans, A. G., Linzer, M. and Russell, L. R., (1974), "Acoustic Emission and Crack Propagation in Polycrystalline Alumina", Mats. Sci. & Eng., 15, 253.
- Evans, A. G. and Nadler, H., (1976), "An Acoustic Emission Study of the Fracture of Zinc Selenide", Mats. Sci. & Eng., 22, 7.
- Graham, L. J. and Alers, G. A., (1973), "Microstructural Aspects of Acoustic Emission Generation in Ceramics", Fracture Mechanics of Ceramics, Vol. 1, Plenum Press, N. Y., p. 175.
- Head, A. K., (1953), "Edge Dislocations in Inhomogeneous Media", Proc. Soc. of London, 796.
- Hildebrand, F. B., (1952), Methods of Applied Mathematics, Prentice Hall, N. Y.
- Mathews, J. R., McClintock, F. A., and Shack, W. J., (1976), "Statistical Determination of Flaw Density in Brittle Materials", J. Am. Ceram. Soc., 59, 304.
- McClintock, F. A., and Zaverl, F., Jr., (1975), "A Computer Model of the Mechanics and Statistics of Brittle Crack Initiation", to be published, Int. J. of Frac.
- McClintock, F. A. and Mayson, H. J., (1976), "Principal Stress Effects on Brittle Crack Statistics", ASME App. Mech. Conf. (Salt Lake City) Vol. 16.
- Noone, M. J. and Mehan, R. L. (1975), "Observation of Crack Propagation in Polycrystalline Ceramics and its Relationship to Acoustic Emissions", Fracture Mechanics of Ceramics, Vol. 1, R. C. Bradt, Ed., Plenum Press, N. Y., p. 201.



Roy, A., Bauer, C. L., (1975), "Effect of Impurities on the Stability of a Moving Grain Boundary", Acta Met., 23, 957.

Simmons, G., and Wang, H., (1971), Single Crystal Elastic Constants and Calculated Aggregate Properties: A Handbook, MIT Press.

Yan, M. F., Cannon, R. M., and Bowen, H. K. (1975a), "Impurity Drag Theory in Grain Boundary Migration of KCl and KBr", in N. J. Grant et al, Research on Materials for High Power Laser Windows, AFCRL-TR-76-0027.

Yan, M. F., Cannon, R. M. and Bowen, H. K. (1975b), "Substructure Formation in Hot Forged KCl and KBr", in N. J. Grant et al., Research on Materials for High Power Laser Windows, AFCRL-TR-76-0027.



# METRIC SYSTEM

## BASE UNITS:

Quantity	Unit	SI Symbol	Formula
length	metre	m	...
mass	kilogram	kg	...
time	second	s	...
electric current	ampere	A	...
thermodynamic temperature	kelvin	K	...
amount of substance	mole	mol	...
luminous intensity	candela	cd	...

## SUPPLEMENTARY UNITS:

plane angle	radian	rad	...
solid angle	steradian	sr	...

## DERIVED UNITS:

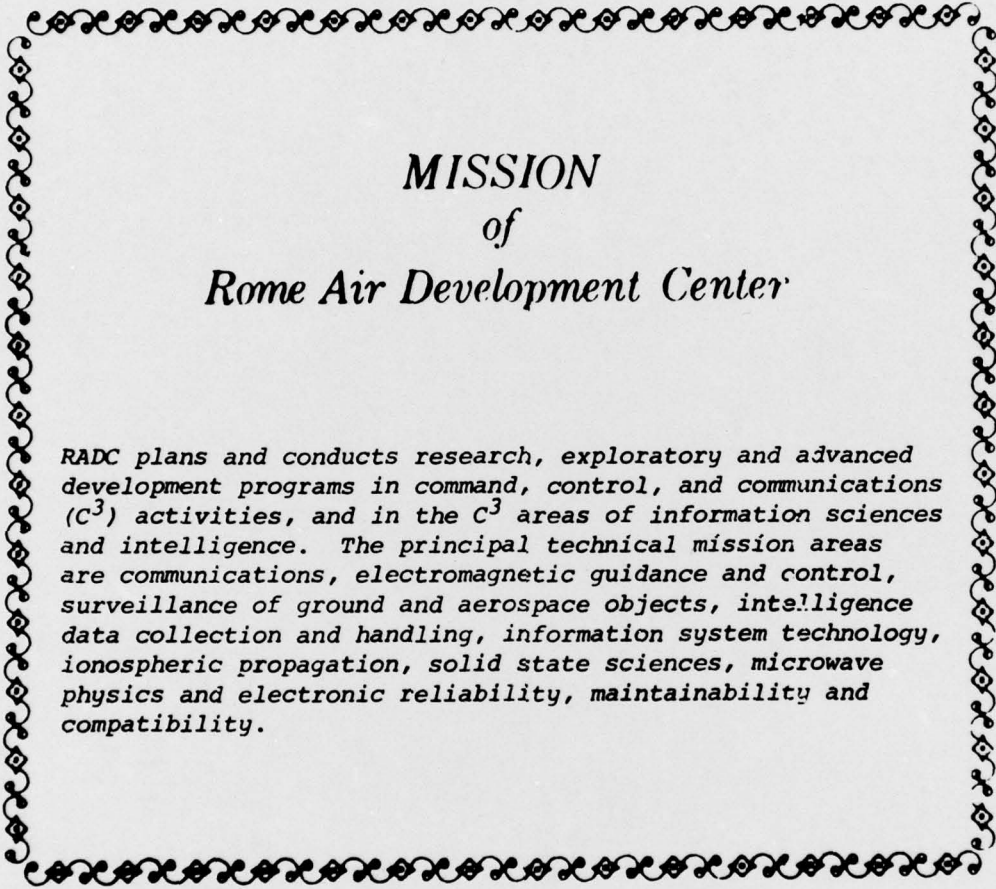
Acceleration	metre per second squared	...	m/s <sup>2</sup>
activity (of a radioactive source)	disintegration per second	...	(disintegration) <sup>s<sup>-1</sup></sup>
angular acceleration	radian per second squared	...	rad/s <sup>2</sup>
angular velocity	radian per second	...	rad/s
area	square metre	...	m <sup>2</sup>
density	kilogram per cubic metre	...	kg/m <sup>3</sup>
electric capacitance	farad	F	A <sup>2</sup> /V
electrical conductance	siemens	S	A/V
electric field strength	volt per metre	...	V/m
electric inductance	henry	H	V <sup>2</sup> /A
electric potential difference	volt	V	W/A
electric resistance	ohm	...	V/A
electromotive force	volt	V	W/A
energy	joule	J	N <sup>2</sup> /m
entropy	joule per kelvin	...	J/K
force	newton	N	kg <sup>2</sup> /m <sup>2</sup> s <sup>2</sup>
frequency	hertz	Hz	(cycle)/s
illuminance	lux	lx	lm/m <sup>2</sup>
luminance	candela per square metre	...	cd/m <sup>2</sup>
luminous flux	lumen	lm	cd <sup>2</sup> sr
magnetic field strength	ampere per metre	...	A/m
magnetic flux	weber	Wb	V <sup>2</sup> s
magnetic flux density	tesla	T	Wb/m <sup>2</sup>
magnetomotive force	ampere	A	...
power	watt	W	J/s
pressure	pascal	Pa	N/m <sup>2</sup>
quantity of electricity	coulomb	C	A <sup>2</sup> s
quantity of heat	joule	J	N <sup>2</sup> /m
radiant intensity	watt per steradian	...	W/sr
specific heat	joule per kilogram-kelvin	...	J/kg <sup>2</sup> K
stress	pascal	Pa	N/m <sup>2</sup>
thermal conductivity	watt per metre-kelvin	...	W/m <sup>2</sup> K
velocity	metre per second	...	m/s
viscosity, dynamic	pascal-second	...	Pa <sup>2</sup> s
viscosity, kinematic	square metre per second	...	m <sup>2</sup> /s
voltage	volt	V	W/A
volume	cubic metre	...	m <sup>3</sup>
wavenumber	reciprocal metre	...	(wave)/m
work	joule	J	N <sup>2</sup> /m

## SI PREFIXES:

Multiplication Factors	Prefix	SI Symbol
1 000 000 000 000 = 10 <sup>12</sup>	tera	T
1 000 000 000 = 10 <sup>9</sup>	giga	G
1 000 000 = 10 <sup>6</sup>	mega	M
1 000 = 10 <sup>3</sup>	kilo	k
100 = 10 <sup>2</sup>	hecto*	h
10 = 10 <sup>1</sup>	deka*	da
0.1 = 10 <sup>-1</sup>	deci*	d
0.01 = 10 <sup>-2</sup>	centi*	c
0.001 = 10 <sup>-3</sup>	milli	m
0.000 001 = 10 <sup>-6</sup>	micro	μ
0.000 000 001 = 10 <sup>-9</sup>	nano	n
0.000 000 000 001 = 10 <sup>-12</sup>	pico	p
0.000 000 000 000 001 = 10 <sup>-15</sup>	femto	f
0.000 000 000 000 000 001 = 10 <sup>-18</sup>	atto	a

\* To be avoided where possible.



A decorative rectangular border with a repeating scrollwork pattern surrounds the central text.

## *MISSION of Rome Air Development Center*

*RADC plans and conducts research, exploratory and advanced development programs in command, control, and communications (C<sup>3</sup>) activities, and in the C<sup>3</sup> areas of information sciences and intelligence. The principal technical mission areas are communications, electromagnetic guidance and control, surveillance of ground and aerospace objects, intelligence data collection and handling, information system technology, ionospheric propagation, solid state sciences, microwave physics and electronic reliability, maintainability and compatibility.*

Printed by  
United States Air Force  
Hanscom AFB, Mass. 01731